# Nanoscale Lamellar Monoclinic Li_2MnO_3 Phase with Stacking Disordering in Lithium-Rich and Oxygen-Deficient $Li_{1.07}Mn_{1.93}O_{4-\delta}$ Cathode Materials

Zhongling Xu,[†] Jianbo Wang,*,[†] Ke Zhang,[†] He Zheng,[†] Zhong-Xu Dai,[†] Jianian Gui,[†] and Xiao-Qing Yang[‡]

[†]School of Physics and Technology, Center for Electron Microscopy and MOE Key Laboratory of Artificial Micro- and Nano-structures, Wuhan University, Wuhan 430072, China

[‡]Brookhaven National Laboratory, Upton, New York 11973, United States

S *Supporting Information*
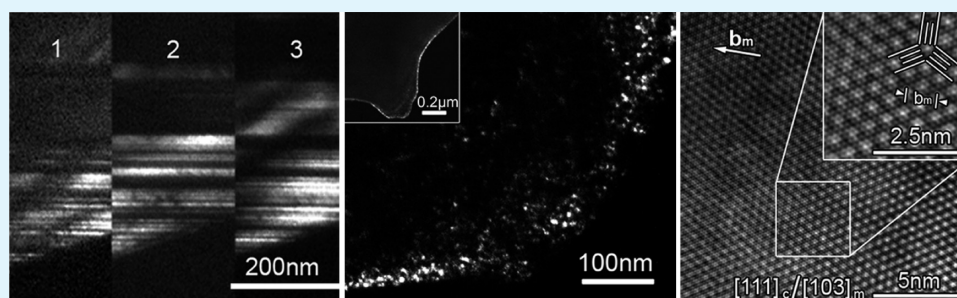
ABSTRACT: The powdered crystalline samples of nominal composition $Li_{1.07}Mn_{1.93}O_{4-\delta}$ have been investigated by transmission electron microscopy (TEM) combined with X-ray powder diffraction (XRD) at room temperature. As suggested by the TEM observation, the dominant phase of the particles is a cubic spinel $Li_{1+\alpha}Mn_{2-\alpha}O_{4-\delta}$ with space group $Fd\overline{3}m$. A monoclinic Li_2MnO_3 phase with $C2/m$ space group was also identified. Furthermore, the occurrence of nanoscale rotational twinning domains in Li_2MnO_3 with 120° rotation angles, stacked along the $[103]_m/[111]_c$ ("m" and "c" represent the monoclinic and cubic descriptions, respectively) axis was also observed. These nanoscale rotational twining domains are responsible for the pseudo-3-fold axis and their formation is supported by the superstructure reflections in selected-area electron-diffraction (SAED) patterns. Similar patterns were reported in the literature but may have been misinterpreted without the consideration of such domains. Consistent with the TEM observation, the XRD results reveal the increasing percentage of monoclinic Li_2MnO_3 with increasing annealing time, associated with more oxygen vacancies. In addition, the electron beam irradiation during TEM studies may cause the nucleation of nanoscale cubic spinel Li−Mn−O crystallites on the monoclinic Li_2MnO_3 grains. These results provide the detailed structural information about the $Li_{1.07}Mn_{1.93}O_{4-\delta}$ samples and advance the understanding of corresponding electrochemical properties of this material as well as other layer structured cathode materials for lithium-ion batteries.

KEYWORDS: phase transition, lithium manganese oxide, monoclinic, domain, oxygen vacancy, transmission electron microscopy, lithium-ion batteries

1. INTRODUCTION

Because of its low cost and high rate capability, the cubic spinel structured $LiMn_2O_4$ (see Figure S1a in the Supporting Information) is considered as one of the most promising cathode materials for lithium-ion batteries to replace those widely used in commercial cells such as $LiCoO_2$ or $LiNiO_2$. Unfortunately, its application as cathode material has been limited by capacity fading during cycling especially at high temperature, due to the dissolution of manganese and Jahn−Teller distortion.[1] In efforts to improve capacity retention, Li-rich non-stoichiometric $Li_{1+\alpha}Mn_{2-\alpha}O_4$ has attracted significant attention since the higher average manganese valence (> +3.5) compared to the stoichiometric counterpart, could suppress Jahn−Teller distortion and improve the cycle stability.[2]

However, it was reported that oxygen vacancies that induce phase transitions during cycling are harmful for the cycling performance of $Li_{1+\alpha}Mn_{2-\alpha}O_{4-\delta}$.[3−5] For instance, a cubic-to-tetragonal phase transition was observed in $Li_{1+\alpha}Mn_{2-\alpha}O_{4-\delta}$ annealed and quenched from high temperature (>800 °C), which is related to cooperative Jahn−Teller distortion induced by local structure defects, especially oxygen vacancies.[6,7] Yang et al.[8] have systematically studied the behavior of $Li_{1.07}Mn_{1.93}O_{4-\delta}$ and proposed that the oxygen deficiency is the key factor controlling this phase transition. The greater δ

value corresponds to the higher phase transition temperature.[8] Although many methods have been developed to reduce these oxygen vacancies, the detailed mechanism of capacity loss and related structural changes have not been thoroughly studied. Since the phases of these materials are closely related to the synthesis conditions and treatment history, a systematic investigation on the relationship between the crystal structures and the treatment history as well as the relationship among different phases is urgently required for the evaluation of electrochemical/physical properties.

Recently, a new type of lithium-rich layer structured cathode material has attracted extensive attentions. These materials with a general formula of $Li[Li_x(TM)_yMn_{1-x-y}]O_2$, where TM stands for transition metal including Mn, Ni, Co, Cr, Fe, etc., or their combinations,[9−20] have high capacity (typically around 250 mAh/g), low cost, excellent structural stability, and capacity retention on cycling.[10,21−23] The structural details of these materials have been under heated debate, i.e., whether they are "real uniform solid solution" without phase separation[15,24] or "composite" compounds in which layered Li_2MnO_3 and $LiTMO_2$ domains are structurally integrated on nanoscale with a shared common oxygen sublattice (better described as $Li_2MnO_3 \cdot LiTMO_2$).[10,12−14,16] Recent studies showed that they are "composite" compounds.[25,26] The Li_2MnO_3 material itself has also been extensively investigated as a potential cathode material. Recent studies showed that Li_2MnO_3 synthesized with optimized strategy exhibits excellent electrochemical performance and yields a reversible capacity up to 200 mAh/g or more.[27−30] It was also reported that Li_2MnO_3 can be activated when delithiated electrochemically by overcharging to high voltages beyond 4.5 V[29] or chemically by acid leaching.[21,32,33] Such products have unexpected capacity and much better stability than that of layered $LiMnO_2$.[21,32−34] The structures of both materials $Li[Li_x(TM)_yMn_{1-x-y}]O_2$ and Li_2MnO_3 are associated with different stacking schemes of TM layers, leading to distinct structures/space groups,[9] i.e., $C2/m$,[35−37] $C2/c$,[38] and $P3_112$[39] (see Figure S1b, c in the Supporting Information). Because of the negligible energy differences among these three structures,[35] similar X-ray powder diffraction (XRD) peaks and selected-area electron-diffraction (SAED) patterns, discrepancies on the structures of these materials still exist. Specifically, based on SAED analysis, Meng et al.[39,40] proposed that $Li[Ni_xLi_{1/3-2x/3}Mn_{2/3-x/3}]O_2$ samples have a $P3_112$ stacking, whereas other researchers reported that the structures of Li_2MnO_3 and $Li_{1.2}Ni_{0.2}Mn_{0.6}O_2$ should be better described as monoclinic $C2/m$ structure using transmission electron microscopy (TEM) and scanning transmission electron microscopy studies.[9,24,37,41] Therefore, further structural studies will provide more valuable information about the related electrochemical performance.[42]

As the spinel $LiMn_2O_4$ has a close structural relationship with the layered Li_2MnO_3 and the "composite" materials $Li[Li_x(TM)_yMn_{1-x-y}]O_2$,[27−29,31,32,43−47] a systematic study on the relationship between the spinel and layered materials should be useful and worthwhile. Because of the close structural similarity among the Mn-based materials, care must be taken in interpreting the XRD and neutron diffraction (ND) patterns. Meanwhile, secondary phases consisting of a small proportion of the sample can hardly be detected applying the XRD or ND techniques. However, high spatial resolution TEM techniques allow us to unambiguously distinguish the phases by checking individual particles in multiphase samples and identify the crystal structure details at the same time. In this paper, using

$Li_{1+\alpha}Mn_{2-\alpha}O_{4-\delta}$ as a model compound, the structural relationship between the cubic spinel and layered phases has been thoroughly investigated using TEM techniques including SAED, dark field imaging (DF), and high-resolution transmission electron microscopy (HRTEM). In addition to the predominant cubic spinel phase, an important secondary phase with Li_2MnO_3 formula and monoclinic symmetry is identified, which has never been discovered in previous studies.[4,6−8] Furthermore, the superstructure reflections in SAED patterns suggest the existence of 120° rotational twinning variants in Li_2MnO_3 with space group of $C2/m$. The structural relationship between Li_2MnO_3 and spinel phase is discussed as well. The discovery of the Li_2MnO_3 with faulted structure in these $Li_{1+\alpha}Mn_{2-\alpha}O_{4-\delta}$ materials provides important structural origins of the oxygen vacancy effects on the electrochemical and magnetic properties.

2. EXPERIMENTAL SECTION

The $Li_{1.07}Mn_{1.93}O_{4-\delta}$ samples in the current work were treated in the same way as those reported by Yang et al.[8] Samples were annealed in pure argon gas at 660 °C for various durations and labeled accordingly. To be specific, F0h represents the material without annealing, whereas F1h, F2h, F3h, F4h, and F12h stand for samples annealed for 1, 2, 3, 4, and 12 h, respectively. On the basis of the thermogravimetric analysis results,[8] the δ values of the oxygen vacancy are 0, 0.131, 0.153, 0.167, 0.182, and 0.299 for samples F0h, F1h, F2h, F3h, F4h, and F12h, respectively. Evidently, with the increasing annealing time, more oxygen vacancies were produced. To prepare samples for TEM observation, a given specimen was mixed with epoxy resin and then injected into a copper tube with external diameter of 3 mm. The mixture was solidified and integrated firmly into the tubes after heating in an oven at 80 °C for 10 h. Then, the tubes containing the mixture were sliced into discs which were mechanically polished and dimpled to less than 40 μm thick. The discs were perforated with argon by a Precision Ion Polishing System (model 691, Gatan, USA) with the acceleration voltage less than 2.7 kV to minimize heating and other potential damage. SAED and DF were obtained in JEOL JEM-2010 (HT) TEM while HRTEM was performed in JEOL JEM-2010 (FEF) TEM with Ω energy filter and field emission gun. Both microscopes were operated at 200 kV. Conventional XRD was carried out on D8 Advance (Bruker AXS inc.) X-ray diffractometer with Cu Kα radiation.

3. RESULTS AND DISCUSSION

3.1. Dominant Cubic Spinel Phase. The cubic spinel $Li_{1.07}Mn_{1.93}O_4$ was found to be the only phase in F0h sample as evidenced by the perfect match between the experimental (Figure 1a) and simulated (Figure 1b) electron diffraction patterns (EDPs). The emergence of some forbidden reflections such as {200} is due to the double diffraction effect. In addition, the cubic spinel phase was the dominant phase in each of the annealed samples, i.e., F1h, F2h, F3h, F4h, and F12h.

3.2. Formation of Secondary Monoclinic Phase and Its Structural Relationship with the Original Spinel Phase. In addition to the original spinel phase, a secondary crystal phase was detected in all of the annealed F1h, F2h, F3h, F4h, and F12h samples. The typical EDPs obtained from sample F4h shown in Figure 2 can be preindexed based on the cubic spinel structure as compared with the EDPs presented in Figure 1, implying the structural similarity between the two phases. However, concerning an EDP of cubic spinel structure (Figure 1), all reciprocal vectors {440} are divided into two parts by {220} (e.g. $[\bar{1}11]$ diffraction pattern in Figure 1), while in Figure 2, certain reciprocal vectors {440}$_c$ (the subscript "c" denotes the cubic description hereafter) are divided by two weak diffractions located at 1/3{440}$_c$ and 2/3{440}$_c$ (e.g.,
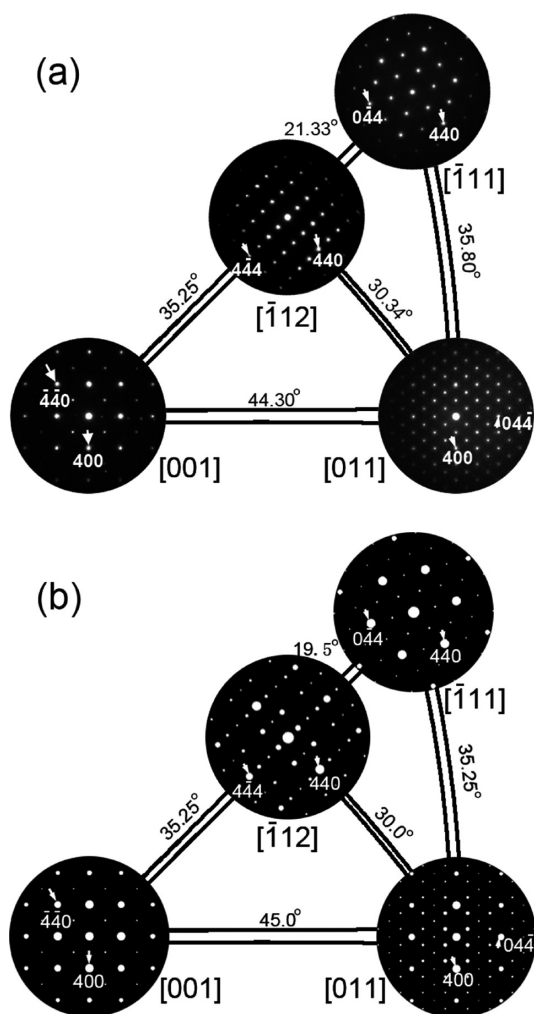
Figure 1. (a) Experimental and (b) simulated EDPs of cubic spinel phase, respectively.

$$\begin{pmatrix} \mathbf{a}_m^* \\ \mathbf{b}_m^* \\ \mathbf{c}_m^* \end{pmatrix} = \begin{pmatrix} 1 & 1 & -1 \\ -2/3 & 2/3 & 0 \\ 1 & 1 & 1 \end{pmatrix} \begin{pmatrix} \mathbf{a}_c^* \\ \mathbf{b}_c^* \\ \mathbf{c}_c^* \end{pmatrix} \tag{1}$$

Hence, the relationship between the basic vectors of two phases in the real space can be deduced

$$\begin{pmatrix} \mathbf{a}_m \\ \mathbf{b}_m \\ \mathbf{c}_m \end{pmatrix} = \begin{pmatrix} 1/4 & 1/4 & -1/2 \\ -3/4 & 3/4 & 0 \\ 1/4 & 1/4 & 1/2 \end{pmatrix} \begin{pmatrix} \mathbf{a}_c \\ \mathbf{b}_c \\ \mathbf{c}_c \end{pmatrix} \tag{2}$$

Taking the lattice parameters of cubic phase of $\mathbf{a}_c = \mathbf{b}_c = \mathbf{c}_c = 8.25$ Å, the lattice parameters of the monoclinic phase are thus estimated to be: $\mathbf{a}_m = 5.05$ Å, $\mathbf{b}_m = 8.75$ Å, $\mathbf{c}_m = 5.05$ Å; $\beta_m = 109.47°$. The lattice parameters we obtained here are quite close to those reported by Strobel et al.[36] for the monoclinic Li_2MnO_3 structure with $C2/m$ space group using single-crystal X-ray diffraction: $\mathbf{a}_m = 4.94$ Å, $\mathbf{b}_m = 8.53$ Å, $\mathbf{c}_m = 5.03$ Å; $\beta_m = 109.46°$. In addition, as the secondary phase derived from $Li_{1+\alpha}Mn_{2-\alpha}O_{4-\delta}$, Li_2MnO_3 is the only Li−Mn−O compound with such structure. Consequently, it is believed that the secondary phase observed in our annealed samples corresponds to the monoclinic layered Li_2MnO_3.

According to the group theory, phase transition from cubic spinel phase with higher symmetry $Fd\bar{3}m$ to monoclinic layered phase with lower symmetry $C2/m$ is accompanied by the loss of 3-fold symmetry along $[111]_c$, which would generate domains linked by the lost 3-fold symmetry and reproduce a pseudo-3-fold symmetry in EDPs, as shown in Figure 2. Taking DF results (Figure 3) into consideration, it is reasonable to assume that the EDPs in Figure 2 result from the combination of three rotational twinning variants with 120° rotation angles, defined by stacking faults of $(111)_c/(001)_m$ plane in monoclinic Li_2MnO_3 crystal phase, which is low in energy penalty[35] for the layered material and cause the pseudo-3-fold axis along $[111]_c$ (i.e., $[103]_m$) direction as seen in Figure 2. To confirm this assumption, using the kinematical theory, three sets of EDPs based on the single-crystal Li_2MnO_3 from each of the three rotational variants along the corresponding zone axes are simulated and presented in Figure 5a−c, respectively. Figure 5d is the superposition of the corresponding EDPs shown in Figure 5a−5c, showing excellent agreement with the observed experimental EDPs in Figure 2, especially the characteristic streaking feature of close arranged weak spots observed along the $[\bar{1}\bar{1}2]_c$ direction.

Most of the EDPs can be well-explained based upon the coexistence of rotational twinning variants, except some remote zone axes. Figure 6 compares three experimental EDPs with their simulated ones. The weak reflections indicated by the long arrows in the experimental EDPs (Figure 6a, e, and g) are absent in the corresponding simulated patterns (Figure 6b, f, and h). These extra spots can be explained as the results of the intersection of streaks of the elongated spots with the reciprocal planes (or Ewald's Sphere). Panels c and d in Figure 6 schematically illustrate the way that the extra spots in Figure 6a were generated. The sites 1, 2, and 3 in Figure 6c and 4, 5, and 6 in Figure 6d marked by short arrows correspond to the numbered spots in Figure 6a, respectively. It can be seen that reflections marked 2 and 5 are inherent reflections, whereas reflections 1 and 4 are caused by the elongation of the close arranged weak spots. Simultaneously, multiple diffraction effect
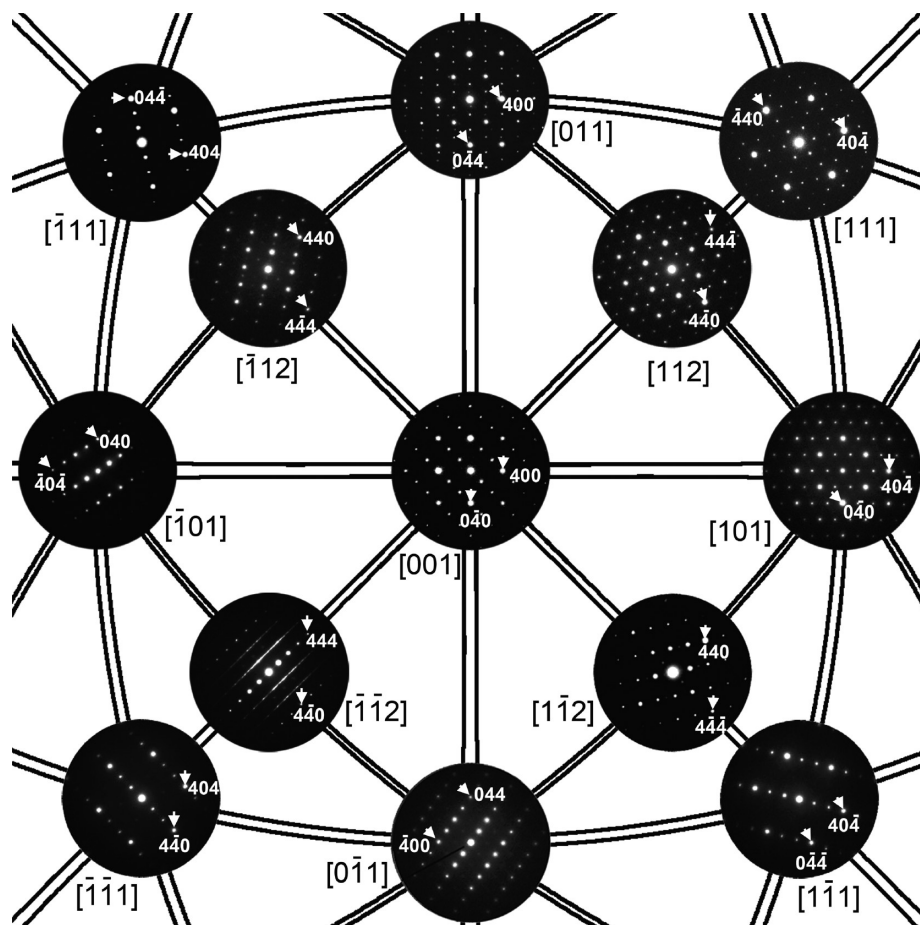
$[111]_c$ diffraction pattern in Figure 2) into three equal parts. Thus, the EDPs shown in Figure 2 indicate a phase with distinct structure other than the cubic spinel phase. One characteristic feature of the EDPs is the streaking along $[111]_c$ observed in $[\bar{1}\bar{1}2]_c$ zone axis, which implies the existence of planar defects or domain boundaries in $(111)_c$. DF technique was applied to identify the regions located in the area of the sample corresponding to certain superstructure diffraction spots. The results in Figure 3 show that the $[\bar{1}\bar{1}2]_c$ EDP consisted of three sets of EDPs originated from three different types of domains or variants in the sample area. It is noted that none of these three component patterns of $[\bar{1}\bar{1}2]_c$ EDP can be indexed by $P3_112$ structure, which was proposed to explain the occurrence of superstructure reflections.[39,40] This suggests that the composite EDP (Figure 2) is a combination of EDPs from three different domains, and when dissembled, the reciprocal lattice of the phase can be achieved by reciprocal lattice reconstruction, as shown in Figure 4. A c-centered monoclinic reciprocal unit cell can be chosen (marked by the masked area in Figure 4) in which $\mathbf{b}_m^*$ (the subscript "m" denotes the monoclinic description hereafter) is the basic vector of unique axis. The relationship between the reciprocal basic vectors of monoclinic and cubic phases can be described as follows

Figure 2. Typical EDPs of a noncubic phase found in the annealed samples. The zone axes and diffraction spots are preliminarily indexed according to the cubic spinel structure.

accounts for the present of weak reflections 3 and 6. Similar mechanism can be applied to explain the occurrence of other extra spots along other remote zone axes in panels e and g in Figure 6.

To reveal the potential relationship between Li_2MnO_3 content and oxygen vacancy value δ of the $Li_{1+\alpha}Mn_{2-\alpha}O_{4-\delta}$, XRD was performed for F0h, F1h, F2h, F3h, F4h, and F12h and the results are plotted in Figure 7. The patterns of different samples were arranged vertically for better analysis. The peaks marked by the asterisks in Figure 7 can be indexed as $\{131\}_m$ and $\{130\}_m$ of Li_2MnO_3. It can be seen clearly that the $\{131\}_m$ and $\{130\}_m$ peaks are not present in the untreated F0h sample. They start to appear in the F1h sample and their intensities become stronger with increasing time, indicating the increased percentage of Li_2MnO_3 phase with more annealing time, associated with greater mass loss and higher oxygen vacancy concentration δ based on the previous thermogravimetric analysis data.[8] This is consistent with the TEM observations that there is more chance to find the Li_2MnO_3 phase in longer annealed samples and previous reports that $Li_{1+\alpha}Mn_{2-\alpha}O_4$ will segregate into the $Li_{1+\beta}Mn_{2-\beta}O_4$ ($\alpha > \beta$) and Li_2MnO_3 with oxygen loss on heating at high temperature.[47,48] However, because of the small content of the Li_2MnO_3 phase and its similar crystal structure with cubic spinel phase, the intensities of characteristic peaks of Li_2MnO_3 are quite weak, making it difficult to get a reliable quantitative percentage of Li_2MnO_3 in our samples. It should be noted that the presence of nanoscale 120° rotational lamellar domains may decrease the intensity of

characteristic monoclinic peaks (e.g., $\{020\}_m$ and $\{110\}_m$) with 2θ between 20 and 35° in the XRD spectrum (CuKα) and make them harder to be detected. The details will be presented in another paper.[49]

The reaction from cubic spinel $Li_{1.07}Mn_{1.93}O_4$ to monoclinic Li_2MnO_3 during annealing can be described as

$$2(1 - \alpha)Li_{1+\alpha}Mn_{2-\alpha}O_4$$
$$= 2(1 - \alpha)Li_{1+\beta}Mn_{2-\beta}O_4 + 2(\alpha - \beta)Li_2MnO_3$$
$$+ (\alpha - \beta)O_2$$
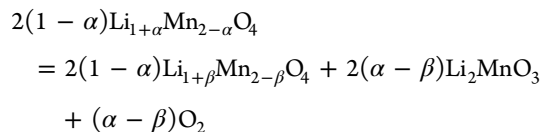
where α and β are the small fractions of octahedra 16d sites occupied by lithium cations in lithium manganese spinel oxides and within the limits $0 \leq \beta < \alpha \leq 1/3$ (in our case, $\alpha = 0.07$). It is evident that, consistent with XRD results, the yield of Li_2MnO_3 is proportionally related to the oxygen loss (or mass loss). Because the monoclinic Li_2MnO_3 is derived from the cubic spinel $Li_{1+\alpha}Mn_{2-\alpha}O_{4-\delta}$ during annealing, it is natural to form lamellar domains oriented along three equivalent orientations in a $\{111\}_c$ plane according to previous analysis, rather than introducing the separated stacking faults as reported in the literature for single-phase Li_2MnO_3.[9,37,50]

These results suggest that the composite EDPs (Figure 2) of Li_2MnO_3 with $C2/m$ structure are ascribed to the 120° rotational stacking of nanoscale Li_2MnO_3 lamellar domains along the $[111]_c/[103]_m$ direction. As the existence of twinning variants will introduce a pseudo-3-fold symmetry in EDPs along
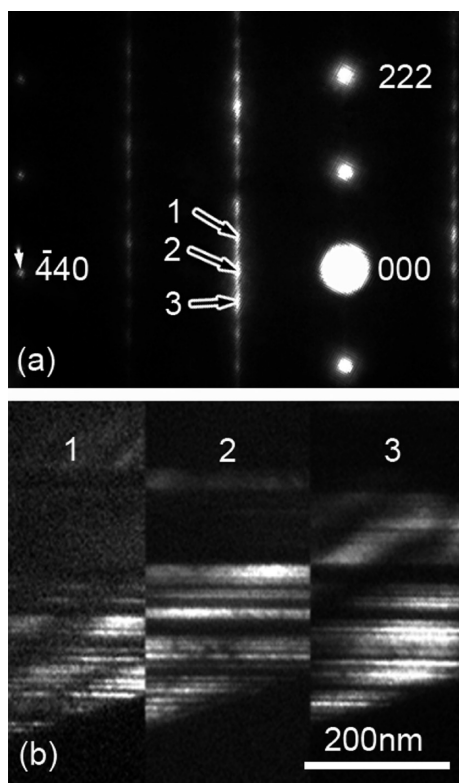
Figure 3. (a) EDP along the $[\overline{1}\overline{1}2]_c$ zone axis shown in Figure 2; (b) DF images of corresponding reflections pointed out in a, suggesting that the EDP is consisted of reflections from three domains in this grain.
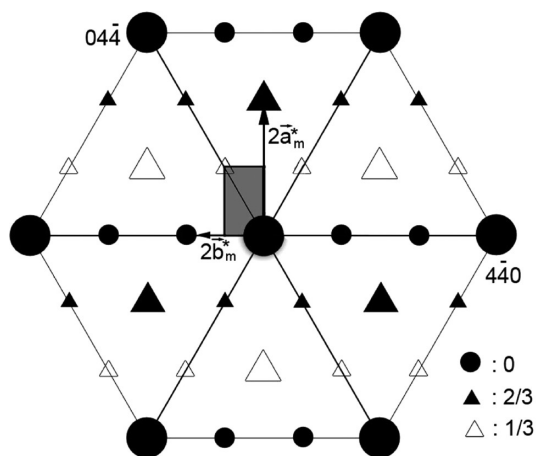

Figure 4. Schematic drawing of the reciprocal lattice of the secondary phase found in the annealed samples. The masked area is the selected monoclinic reciprocal unit cell in which $\mathbf{b}_m^*$ is the unique axis. Different shapes indicate different heights from the horizon and bigger size stands for stronger reflections based on our experimental results.

$[111]_c/[103]_m$ direction that can be easily misinterpreted, it is suggested that the observation direction should be aligned perpendicular to $[111]_c/[103]_m$ (i.e., $[\overline{1}\overline{1}2]_c$) to clearly determine the corresponding structures. Also, because these domains are stacked randomly along the $[111]_c/[103]_m$ axis, it is possible to form local $P3_112$ stacking in a limited number of layers on the boundary of adjacent domains,[39] but they should not be the dominant structure.[51] Therefore, it is better to describe the structure of the heavily faulted Li_2MnO_3 as "$C2/m$

structure with rotational twinning domains and stacking faults" rather than "dominant $C2/m$ structure with local $P3_112$ structure on domain boundary". The streaks along $[111]_c$ observed in $[\overline{1}\overline{1}2]_c$ EDP are due to the domain boundaries in $(111)_c$ instead of the possible point defects or in-plane disorder domains in TM layer[39] in our case. Because this family of layered materials includes Li_2MnO_3 and $Li[Li_xTM_yMn_{1-x-y}]O_2$ with an in-plane ordered $(3)^{1/2}a_{hex} \times (3)^{1/2}a_{hex}$ "honey-comb" superstructure, it is suggested that TEM techniques could be an effective approach to distinguish the $C2/m$ stacking with high concentration of rotational domains from the perfect $P3_112$ structure.

The formation of monoclinic Li_2MnO_3 and its derivatives may have dramatic influence on physical/electrochemical properties of spinel $LiMn_2O_4$. For instance: (1) as Mn^{4+} is a crucial factor for the high voltage behavior of $LiMn_{2-x}TM_xO_4$ materials,[52,53] the potential emergence of Li_2MnO_3 can contribute to the electrochemical performance of the material especially at high operation voltage;[54,55] (2) the lithium cations in Li_2MnO_3 are not active at 4 V during charge-discharge process, the capacity fading in oxygen deficient compounds may partially result from the formation of the inert monoclinic phase Li_2MnO_3 as a product of oxygen loss; (3) the cubic spinel $LiMn_2O_4$ and Li_2MnO_3 have different magnetic behaviors. At present, it is still unclear whether there exists magnetic long-range ordering or not in $LiMn_2O_4$. The unexpected magnetic long-range-ordered Li_2MnO_3 can make things more complex.[56] In addition, the probable presence of Li_2MnO_3 should be taken into consideration concerning the formation and structure of low-temperature $LiMn_2O_4$ phase. The presence of unidentified Li_2MnO_3 will introduce extra peaks which may cover some characteristic peaks of Jahn-Teller distorted phase of $LiMn_2O_4$ and make it difficult to determine whether it has a tetragonal[57] or orthorhombic[58] structure.

3.3. Electron Beam (e-beam) Induced Nucleation of Nanoscale Cubic Spinel $Li_{1+\alpha}Mn_{2-\alpha}O_{4-\delta}$ Crystallites on Monoclinic Grains. With the increasing irradiation time, extra weak spots that can be indexed with cubic spinel $Fd\overline{3}m$ structure gradually appeared in almost all EDPs of the Li_2MnO_3 grains, as marked by arrows in Figure 8a for the F4h sample after about 60 min irradiation. The DF image by selecting $(2\overline{2}0)_c$ spot (Figure 8b) reveals that these diffractions originate from nanoscale domains randomly distributed on the surface and the edge of Li_2MnO_3 grains.

The HRTEM images of Li_2MnO_3 observed along $[111]_c$ and $[110]_c$ directions for the F4h sample exposed under the e-beam for about 90 min are shown in Figure 9. The tripled period of the basic lattice along $[\overline{1}10]_c$, $[01\overline{1}]_c$, and $[10\overline{1}]_c$ directions can be seen in whole areas marked in images a and b in Figure 9, which imply good crystallization and $(3)^{1/2}a_{hex} \times (3)^{1/2}a_{hex}$ intralayer ordering of the Li_2MnO_3 phase. Extra spots which correspond to the cubic spinel structure are also observed in the fast Fourier transform patterns (FFT) of the HRTEM images, as circled in images c and d in Figure 9. Fourier filtered images of the weak diffused spots in images c and d in Figure 9 indicate that the nanosized round shape cubic spinel crystallites are randomly distributed on the surface of Li_2MnO_3 grains (circled areas in Figure 9e, f), coincident with what has been observed in the DF image (Figure 8b). The relationship of crystal orientation between the cubic spinel and monoclinic phase can also be described by eqs 1 and 2.

It is noted that the intensities of this kind of extra reflections become stronger and stronger as the radiation continues,
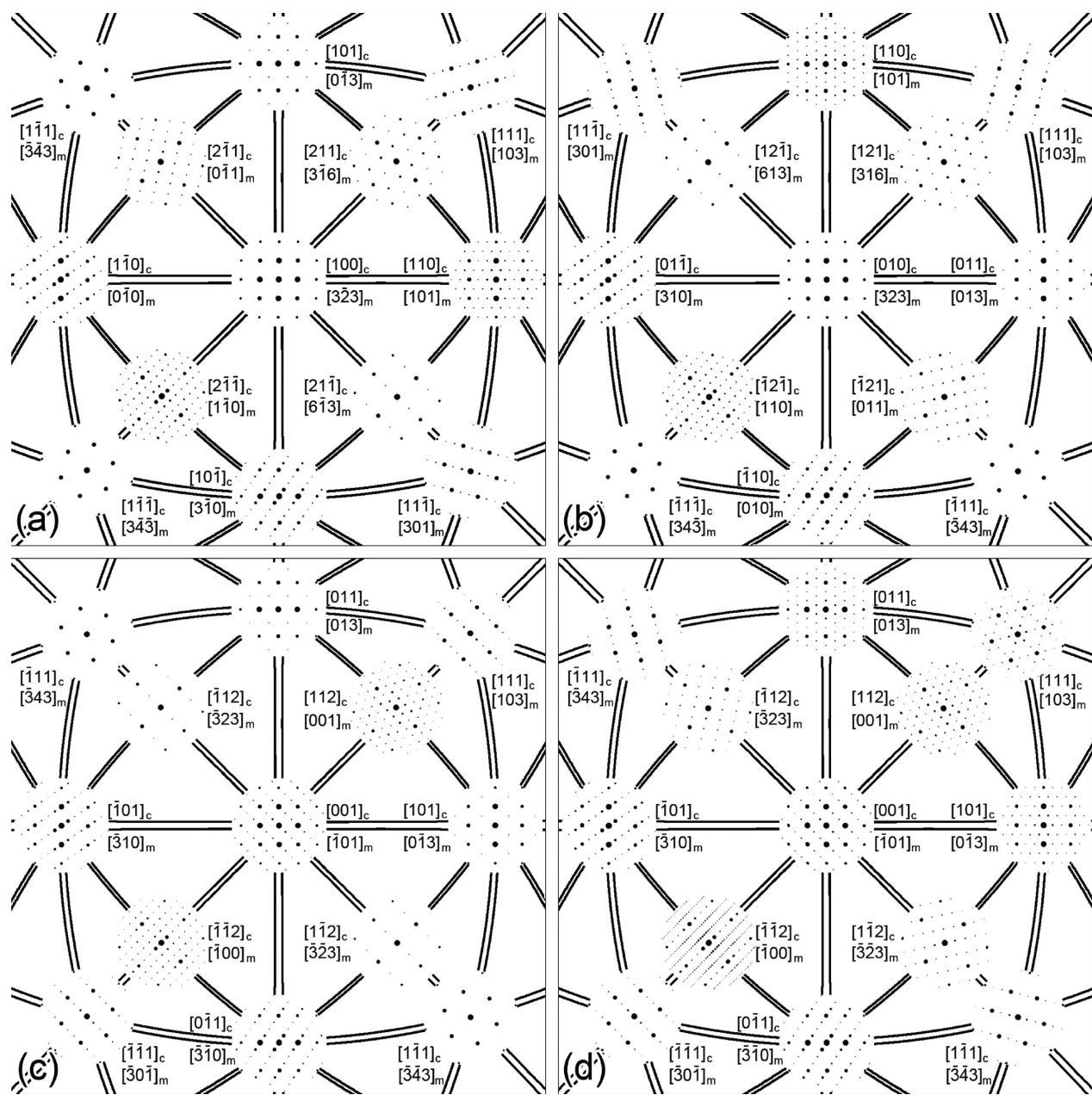
1223

dx.doi.org/10.1021/am404963u | ACS Appl. Mater. Interfaces 2014, 6, 1219–1227

Figure 5. (a–c) Simulated EDPs of three 120° rotational twinning variants of Li_2MnO_3 (SG: $C2/m$), respectively; (d) the superposition EDPs of a–c.

suggesting an e-beam induced monoclinic to cubic spinel phase transition. The lithium and oxygen ions located at the surface area can be easily knocked out under the high energy (200 keV) electron irradiation, changing the element ratios. The surface oxygen loss induced by electron irradiation has been manifested by the lower O/Mn+Fe+O values observed in EELS along the edge in the literature for the $Li_{1.2}Mn_{0.4}Fe_{0.4}O_2$ particles.[12] When the ion ratio $Li^+:Mn^{3+/4+}:O^{2-}$ approaches certain values (i.e., 1:2:4) in certain areas on the Li_2MnO_3 grains, accompanied by "heating effect" of high energy e-beam and sample interaction, the structure of these "damaged" areas could re-arrange into the cubic spinel phase. Thus, long-period electron irradiation should be avoided when identifying the potential cubic spinel phase in layered materials like Li_2MnO_3. This conclusion is consistent with previous report that that acid leached Li_2MnO_3 (with effective loss of Li_2O) will transform

into a spinel phase on subsequent heating.[32] It is worthy of noting that such kind of phase transition may also account for the complicated EDPs that have been observed in other layered cathode materials such as delithiated $Li_{0.5}CoO_2$,[59] $Li_{1.2}Mn_{0.4}Fe_{0.4}O_2$,[13] and $Li_xNi_{0.5}Mn_{0.5}O_2$[60] under e-beam irradiation.

4. CONCLUSIONS

Combining structural studies using both TEM and XRD analysis, a monoclinic Li_2MnO_3 phase with $C2/m$ space group in annealed $Li_{1.07}Mn_{1.93}O_{4-\delta}$ samples has been identified, in addition to the dominant cubic spinel phase. The detailed structural relationship between these two phases is discussed. Interestingly, the 120° rotational nanoscale lamellar stacking domains separated by stacking faults were found in this monoclinic phase, which is hard to be identified by bulk
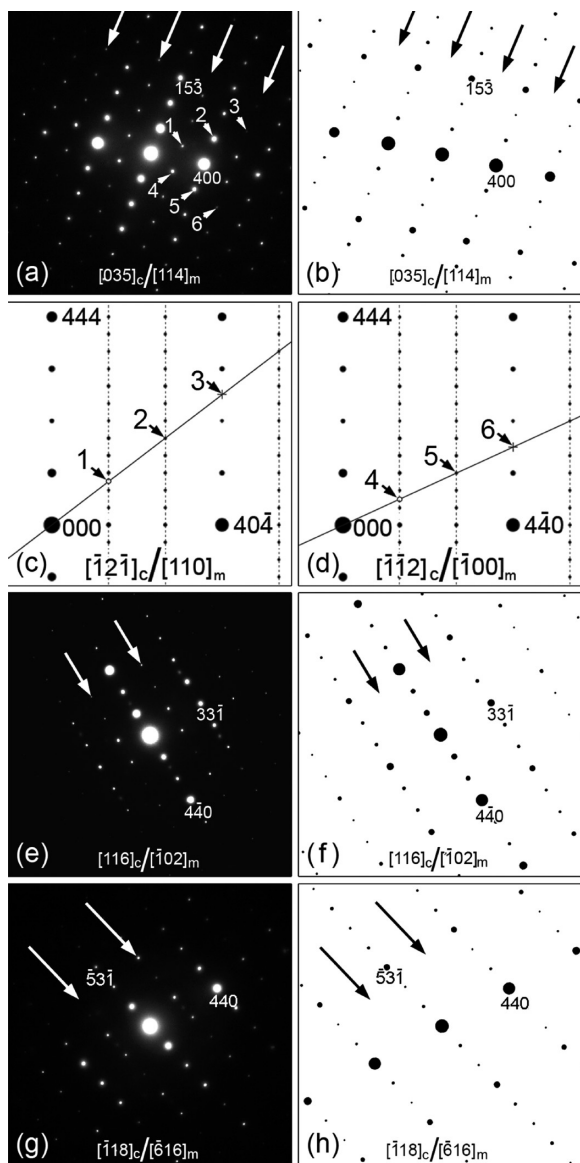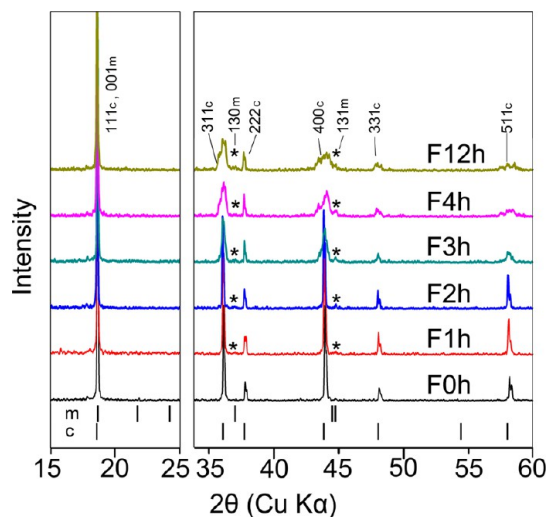
Figure 7. Normalized XRD patterns of F0h, F1h, F2h, F3h, F4h, and F12h. The bars under the curves stand for the reflections positions of monoclinic Li_2MnO_3 (m) and cubic spinel $LiMn_2O_4$ (c), respectively. The asterisks point out the $\{131\}_m$ and $\{130\}_m$ peaks of monoclinic Li_2MnO_3.
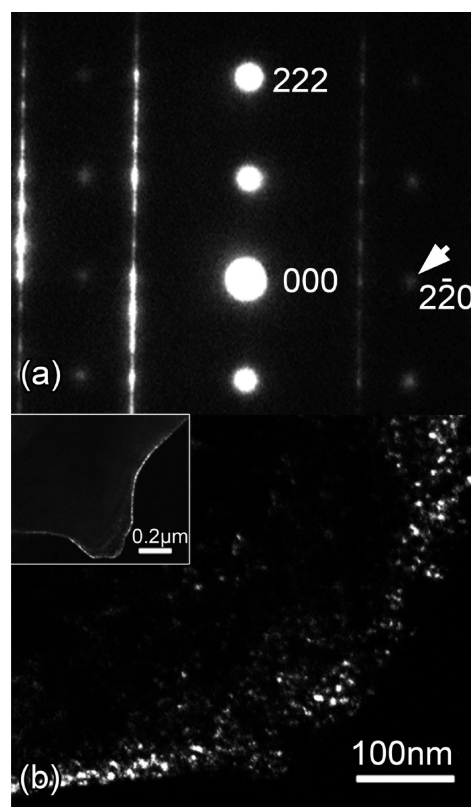

Figure 6. EDPs of (a) $[035]_c/[114]_m$, (e) $[116]_c/[\bar{1}02]_m$, and (g) $[\bar{1}18]_c/[\bar{6}16]_m$ with extra spots (pointed out by long arrows). (b, f, h) Corresponding simulated EDPs, respectively. (c, d) Schematic drawings showing that the extra spots in panel a are generated by cutting the elongated spots. The dashed lines represent the elongation of the spots and the numbered short arrows 1, 2, 3 in c and 4, 5, 6 in d mark the corresponding sites in a with same number.

Figure 8. (a) EDP of $[\bar{1}\bar{1}2]_c/[\bar{1}00]_m$ after TEM observation; (b) DF image of reflection $(2\bar{2}0)_c$, which shows the accretion of nanoscale cubic spinel crystallites spotted on the surface of Li_2MnO_3 grains. Inset shows the lower-magnification DF image of the particle.

analysis techniques like XRD and may introduce apparent pseudo-3-fold rotation axis in single EDP along $[111]_c/[103]_m$ axis.

The similarity in EDPs, orientation relationship between the Li_2MnO_3 domains and cubic spinel $Li_{1+\alpha}Mn_{2-\alpha}O_{4-\delta}$ and XRD results suggest that the monoclinic Li_2MnO_3 was derived from cubic spinel $Li_{1+\alpha}Mn_{2-\alpha}O_{4-\delta}$ during annealing. The transition from cubic spinel $Li_{1+\alpha}Mn_{2-\alpha}O_{4-\delta}$ to monoclinic phase Li_2MnO_3 is closely related to oxygen loss and lithium excess of the materials. Furthermore, the phase transition from monoclinic Li_2MnO_3 to the cubic spinel phase caused by radiation damage of the high-energy e-beam during TEM studies was also observed.

These results provide valuable information about the phase components in lithium rich oxygen deficient $Li_{1+\alpha}Mn_{2-\alpha}O_{4-\delta}$

and the phase transitions/structural relationship between the cubic spinel and layered phases in Li−Mn−O system; and should be helpful for the studies of other structurally related cathode materials like $Li[Li_xTM_yMn_{1-x-y}]O_2$.
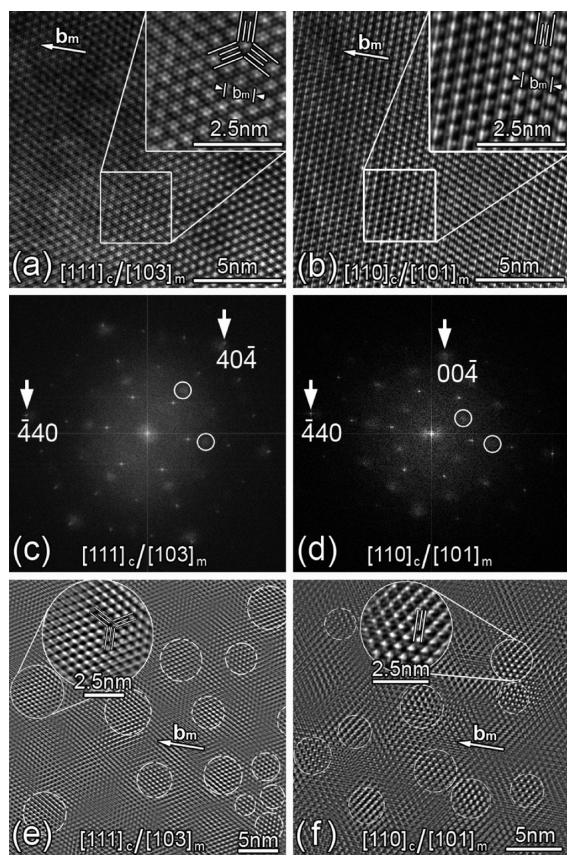
Figure 9. HRTEM of monoclinic Li_2MnO_3 along (a) $[111]_c/[103]_m$ and (b) $[110]_c/[101]_m$. The insets are the magnified views that clearly present the triple period of basic lattice along $[\overline{4}40]_o$, $[40\overline{4}]_o$, and $[04\overline{4}]_o$; (c, d) the FFT images of a and b, respectively. The circles point out reflections corresponding to cubic spinel phase; (e, f) the Fourier filtered images of a and b, respectively. The circled areas represent the location of cubic phase crystallites with doubled period of basic lattice. Insets are the magnification of typical areas.

ASSOCIATED CONTENT

⑤ Supporting Information

Figure S1. This material is available free of charge via the Internet at http://pubs.acs.org.

AUTHOR INFORMATION

Corresponding Author

*E-mail: wang@whu.edu.cn.

Notes

The authors declare no competing financial interest.

ACKNOWLEDGMENTS

REFERENCES

(1) Thackeray, M. M.; Shao-Horn, Y.; Kahaian, A. J.; Kepler, K. D.; Vaughey, J. T.; Hackney, S. A. *Electrochem. Solid-State Lett.* **1998**, *1*, 7−9.

(2) Gummow, R. J.; de Kock, A.; Thackeray, M. M. *Solid State Ionics* **1994**, *69*, 59−67.

(3) Xia, Y.; Zhou, Y.; Yoshio, M. *J. Electrochem. Soc.* **1997**, *144*, 2593−2600.

(4) Xia, Y.; Sakai, T.; Fujieda, T.; Yang, X. Q.; Sun, X.; Ma, Z. F.; McBreen, J.; Yoshio, M. *J. Electrochem. Soc.* **2001**, *148*, A723−A729.

(5) Chida, Y.; Wada, H.; Shizuka, K. *J. Power Sources* **1999**, *81-82*, 454−457.

(6) Tarascon, J. M.; McKinnon, W. R.; Coowar, F.; Bowmer, T. N.; Amatucci, G.; Guyomard, D. *J. Electrochem. Soc.* **1994**, *141*, 1421−1431.

(7) Yamada, A.; Miura, K.; Hinokuma, K.; Tanaka, M. *J. Electrochem. Soc.* **1995**, *142*, 2149−2156.

(8) Yang, X. Q.; Sun, X.; Balasubramanian, M.; McBreen, J.; Xia, Y.; Sakai, T.; Yoshio, M. *Electrochem. Solid-State Lett.* **2001**, *4*, A117−A120.

(9) Bareno, J.; Lei, C. H.; Wen, J. G.; Kang, S. H.; Petrov, I.; Abraham, D. P. *Adv. Mater.* **2010**, *22*, 1122−1127.

(10) Thackeray, M. M.; Kang, S. H.; Johnson, C. S.; Vaughey, J. T.; Benedek, R.; Hackney, S. A. *J. Mater. Chem.* **2007**, *17*, 3112−3125.

(11) Chemova, N. A.; Ma, M.; Xiao, J.; Whittingham, M. S.; Breger, J.; Grey, C. P. *Chem. Mater.* **2007**, *19*, 4682−4693.

(12) Kikkawa, J.; Akita, T.; Tabuchi, M.; Shikano, M.; Tatsumi, K.; Kohyama, M. *Appl. Phys. Lett.* **2007**, *91*, 54103−54105.

(13) Kikkawa, J.; Akita, T.; Tabuchi, M.; Shikano, M.; Tatsumi, K.; Kohyama, M. *J. Appl. Phys.* **2008**, *103*, 104911−104920.

(14) Kim, J.-S.; Johnson, C. S.; Vaughey, J. T.; Thackeray, M. M.; Hackney, S. A.; Yoon, W.; Grey, C. P. *Chem. Mater.* **2004**, *16*, 1996−2006.

(15) Lu, Z.; Chen, Z.; Dahn, J. R. *Chem. Mater.* **2003**, *15*, 3214−3220.

(16) Pan, C.; Lee, Y. J.; Ammundsen, B.; Grey, C. P. *Chem. Mater.* **2002**, *14*, 2289−2299.

(17) Park, C. W.; Kim, S. H.; Mangani, I. R.; Lee, J. H.; Boo, S.; Kim, J. *Mater. Res. Bull.* **2007**, *42*, 1374−1383.

(18) Tabuchi, M.; Nakashima, A.; Ado, K.; Kageyama, H.; Tatsumi, K. *Chem. Mater.* **2005**, *17*, 4668−4677.

(19) Yabuuchi, N.; Kim, Y.-T.; Li, H. H.; Shao-Horn, Y. *Chem. Mater.* **2008**, *20*, 4936−4951.

(20) Yoon, W. S.; Grey, C. P.; Balasubramanian, M.; Yang, X. Q.; McBreen, J. *Chem. Mater.* **2003**, *15*, 3161−3169.

(21) Johnson, C. S.; Korte, S. D.; Vaughey, J. T.; Thackeray, M. M.; Bofinger, T. E.; Shao-Horn, Y.; Hackney, S. A. *J. Power Sources* **1999**, *81-82*, 491−495.

(22) Zeng, D. L.; Cabana, J.; Yoon, W. S.; Grey, C. P. *Chem. Mater.* **2010**, *22*, 1209−1219.

(23) Park, S. H.; Kang, S. H.; Johnson, C. S.; Amine, K.; Thackeray, M. M. *Electrochem. Commun.* **2007**, *9*, 262−268.

(24) Lei, C. H.; Bareño, J.; Wen, J. G.; Petrov, I.; Kang, S. H.; Abraham, D. P. *J. Power Sources* **2008**, *178*, 422−433.

(25) Wen, J. G.; Bareño, J.; Lei, C. H.; Kang, S. H.; Balasubramanian, M.; Petrov, I.; Abraham, D. P. *Solid State Ionics* **2011**, *182*, 98−107.

(26) Bareño, J.; Balasubramanian, M.; Kang, S. H.; Wen, J. G.; Lei, C. H.; Pol, S. V.; Petrov, I.; Abraham, D. P. *Chem. Mater.* **2011**, *23*, 2039−2050.

(27) Park, S. H.; Ahn, H. S.; Park, G. J.; Kim, J.; Lee, Y. S. *Mater. Chem. Phys.* **2008**, *112*, 696−701.

(28) Park, S.-H.; Sato, Y.; Kim, J.-K.; Lee, Y.-S. *Mater. Chem. Phys.* **2007**, *102*, 225−230.

(29) Yu, D. Y. W.; Yanagida, K.; Kato, Y.; Nakamura, H. *J. Electrochem. Soc.* **2009**, *156*, A417−A424.

(30) Jain, G.; Yang, J.; Balasubramanian, M.; Xu, J. *J. Chem. Mater.* **2005**, *17*, 3850−3860.

(31) Robertson, A. D.; Bruce, P. G. *Chem. Mater.* **2003**, *15*, 1984−1992.

(32) Rossouw, M. H.; Thackeray, M. M. *Mater. Res. Bull.* **1991**, *26*, 463−473.

(33) Paik, Y.; Grey, C. P.; Johnson, C. S.; Kim, J. S.; Thackeray, M. M. *Chem. Mater.* **2002**, *14*, 5109−5115.

(34) Tang, W.; Kanoh, H.; Yang, X.; Ooi, K. *Chem. Mater.* **2000**, *12*, 3271−3279.

(35) Bréger, J.; Jiang, M.; Dupré, N.; Meng, Y. S.; Shao-Horn, Y.; Ceder, G.; Grey, C. P. *J. Solid State Chem.* **2005**, *178*, 2575−2585.

(36) Strobel, P.; Lambert-Andron, B. *J. Solid State Chem.* **1988**, *75*, 90−98.

(37) Lei, C. H.; Wen, J. G.; Sardela, M.; Bareño, J.; Petrov, I.; Kang, S. H.; Abraham, D. P. *J. Mater. Sci.* **2009**, *44*, 5579−5587.

(38) Riou, A.; Lecerf, A.; Gerault, Y.; Cudennec, Y. *Mater. Res. Bull.* **1992**, *27*, 269−275.

(39) Meng, Y. S.; Ceder, G.; Grey, C. P.; Yoon, W. S.; Jiang, M.; Bréger, J.; Shao-Horn, Y. *Chem. Mater.* **2005**, *17*, 2386−2394.

(40) Meng, Y. S.; Ceder, G.; Grey, C. P.; Yoon, W. S.; Shao-Horn, Y. *Electrochem. Solid-State Lett.* **2004**, *7*, A155−A158.

(41) Jarvis, K. A.; Deng, Z.; Allard, L. F.; Manthiram, A.; Ferreira, P. J. *Chem. Mater.* **2011**, *23*, 3614−3621.

(42) Yu, H.; Zhou, H. *J. Phys. Chem. Lett.* **2013**, *4*, 1268−1280.

(43) Shao-Horn, Y.; Hackney, S. A.; Armstrong, A. R.; Bruce, P. G.; Gitzendanner, R.; Johnson, C. S.; Thackeray, M. M. *J. Electrochem. Soc.* **1999**, *146*, 2404−2412.

(44) Hong, Y.-S.; Park, Y. J.; Ryu, K. S.; Chang, S. H. *Solid State Ionics* **2005**, *176*, 1035−1042.

(45) Johnson, C. S.; Li, N.; Lefief, C.; Vaughey, J. T.; Thackeray, M. M. *Chem. Mater.* **2008**, *20*, 6095−6106.

(46) Bai, Y.; Wu, C.; Wu, F.; Wang, G.-q. *Trans. Nonferrous Met. Soc. China* **2006**, *16*, 402−408.

(47) Komaba, S.; Yabuuchi, N.; Ikemoto, S. *J. Solid State Chem.* **2010**, *183*, 234−241.

(48) Paulsen, J. M.; Dahn, J. R. *Chem. Mater.* **1999**, *11*, 3065−3079.

(49) Zheng, H.; Wang, J.; Xu, Z.; Wang, R.; Yang, X.-Q. *J. Appl. Crystallogr.* **2013**, submitted.

(50) Boulineau, A.; Croguennec, L.; Delmas, C.; Weill, F. *Chem. Mater.* **2009**, *21*, 4216−4222.

(51) Jarvis, K. A.; Deng, Z.; Allard, L. F.; Manthiram, A.; Ferreira, P. J. *J. Mater. Chem.* **2012**, *22*, 11550−11555.

(52) Kawai, H.; Tabuchi, M.; Nagata, M.; Tukamoto, H.; R. West, A. *J. Mater. Chem.* **1998**, *8*, 1273−1280.

(53) Shao-Horn, Y.; Middaugh, R. L. *Solid State Ionics* **2001**, *139*, 13−25.

(54) Obrovac, M. N.; Gao, Y.; Dahn, J. R. *Phys. Rev. B* **1998**, *57*, 5728.

(55) Shin, Y.; Manthiram, A. *Electrochim. Acta* **2003**, *48*, 3583−3592.

(56) Tomeno, I.; Kasuya, Y.; Tsunoda, Y. *Phys. Rev. B* **2001**, *64*, 094422.

(57) Masquelier, C.; Tabuchi, M.; Ado, K.; Kanno, R.; Kobayashi, Y.; Maki, Y.; Nakamura, O.; Goodenough, J. B. *J. Solid State Chem.* **1996**, *123*, 255−266.

(58) Oikawa, K.; Kamiyama, T.; Izumi, F.; Chakoumakos, B. C.; Ikuta, H.; Wakihara, M.; Li, J.; Matsui, Y. *Solid State Ionics* **1998**, *109*, 35−41.

(59) Shao-Horn, Y.; Levasseur, S.; Weill, F.; Delmas, C. *J. Electrochem. Soc.* **2003**, *150*, A366.

(60) Li, H. H.; Yabuuchi, N.; Meng, Y. S.; Kumar, S.; Breger, J.; Grey, C. P.; Shao-Horn, Y. *Chem. Mater.* **2007**, *19*, 2551−2565.